Compound Metaoptics for Amplitude and Phase Control of Wave Fronts

Brian O. Raeker and Anthony Grbic

Phys. Rev. Lett. **122**, 113901 — Published 22 March 2019

DOI: 10.1103/PhysRevLett.122.113901

Compound Metaoptics for Lossless Amplitude and Phase Control of Wavefronts

Brian O. Raeker and Anthony Grbic
Department of Electrical Engineering and Computer Science, University of Michigan, Ann Arbor, MI 48109-2122 USA

Metasurfaces allow tailored control of electromagnetic wavefronts. However, due to the local conservation of power flow, passive, lossless, and reflectionless metasurfaces have been limited to imparting phase discontinuities – and not power density discontinuities – onto a wavefront. Here, we show how the phase and amplitude profiles of a wavefront can be independently controlled using two closely-spaced, phase-discontinuous metasurfaces. The two metasurfaces, each designed to exhibit spatially-varying refractive properties, are separated by a wavelength-scale distance and together form a compound metaoptic. A method of designing the compound metaoptic is presented, which enables transformation between arbitrary complex-valued field distributions without reflection, absorption, polarization loss, or active components. Such compound metaoptics may find applications in the optical trapping of particles, displaying three-dimensional holographic images, shrinking the size of optical systems, or producing custom (shaped and steered) far-field radiation patterns.

Metasurfaces are two-dimensional arrays of sub-wavelength polarizable inclusions, which aggregately manipulate an electromagnetic wave [1–3]. These inclusions, or unit cells, are arranged in single- or few-layer stacks that are electrically/optically thin. In general, the electromagnetic interactions of a metasurface can be approximated as surface boundary conditions, simplifying analysis and design. A distinct application of metasurfaces is their ability to impart tailored phase discontinuities onto incident wavefronts, demonstrating functions such as focusing, refraction, and polarization control [4–7].

If a metasurface is restricted to be passive, lossless, and reflectionless, the local power density of an incident wave normal to the surface is maintained when transmitted through the metasurface. We denote this local power density normal to a surface as the local power flux through the surface. Such metasurfaces exhibit high transmission efficiency, but only reshape the phase profile of an incident wavefront and not its local power flux profile [7–10]. As a result, a single phase-only metasurface cannot independently control the phase and amplitude distributions of the transmitted field. Specifically, this can result in speckle noise (random fluctuations in amplitude) in holographic images formed with a phase-only surface [11, 12]. Amplitude and phase control over an incident wavefront can suppress speckle, as shown by complex-valued holograms [13–15]. However, such field control has not been demonstrated using reflectionless metasurfaces free of absorption and polarization losses.

Different methods of controlling the amplitude and phase of electromagnetic fields using metamaterials have been reported. In [16], a method for determining material parameters supporting independently defined amplitude and phase field characteristics was introduced. However, loss and gain parameters were necessary to implement the desired field. In [17], a lossless, passive, and reflectionless anisotropic metamaterial was used to form a desired complex-valued field by manipulating the phase and power flow within the medium. These approaches, however, require a metamaterial medium, which can be challenging to fabricate. Additionally, leaky-wave structures [18–20] and partially reflecting cavities [21–23] can also create complex-valued aperture fields, but generate reflections which could interact with the source.

Phase and amplitude control has been demonstrated with partially reflective or lossy metasurfaces. In [12, 13, 24–27] the desired field profile is produced on the transmitted, cross-polarized field. In these cases polarization loss is used to form the desired phase and amplitude patterns. In [28, 29] the amplitude of the transmitted co-polarized field is controlled through absorption loss. Each of these demonstrations applies a form of loss (reflection, absorption, or polarization) to implement the desired field. Therefore, the total transmitted power is decreased in exchange for amplitude control. In contrast to these earlier works, we propose passive, lossless, and reflectionless compound metaoptics for arbitrary wavefront reshaping in terms of both amplitude and phase for the desired polarization. Specifically, reflection, absorption, and polarization losses are avoided and all available incident power is used to form the desired field pattern.

A compound metaoptic is a collection of individual metasurfaces arranged along an axis, analogous to an optical compound lens. With additional degrees of freedom, compound metaoptics can achieve electromagnetic responses difficult or impossible to achieve with a single metasurface. We propose using reflectionless metasurfaces, illustrated in Fig. 1, to achieve both phase control (beam steering) and amplitude control (beam shaping) in a low-loss, low-profile manner. This approach promises higher diffraction efficiencies than conventional holograms since both amplitude and phase are controlled with sub-wavelength pixelation.

The metasurfaces act as two phase planes: two reflectionless, inhomogeneous surfaces that manipulate the phase of the transmitted wavefront. Together, the two phase planes provide two degrees of freedom to control two wavefront attributes: the amplitude and phase pro-

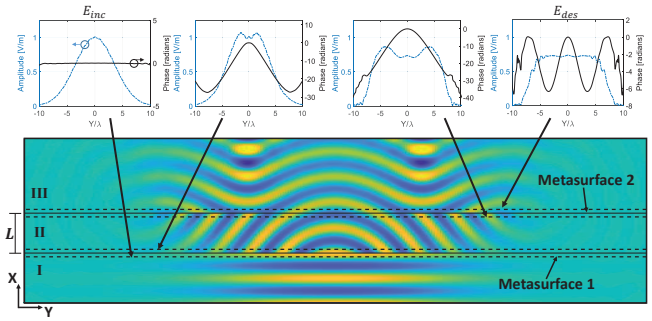

FIG. 1. Two metasurfaces form the compound metaoptic, establishing three regions. The phase-discontinuous metasurfaces reshape the amplitude and phase profiles of an incident beam, as demonstrated by the wavefront behavior. The inset plots display the amplitude and phase profiles before and after each metasurface. Local power flux through each metasurface is conserved, eliminating reflections.

files. In the proposed arrangement, the first metasurface reshapes the incident field power flux to form the desired power flux profile at the second metasurface. The second metasurface provides a phase-correction to establish the desired amplitude and phase profiles. The method is scalable from microwave to visible wavelengths.

Related methods of forming desired complex-valued optical fields have used reflective spatial light modulators [30] or deformable mirrors [31]. The spatial light modulators or mirrors are located at conjugate Fourier planes of a two-lens optical system, limiting its compactness. Even lensless systems are still large due to the use of reflective components [32]. The custom phase-discontinuity profiles implemented by the metasurfaces avoid the need for lenses and reflective components. This provides a significantly more low-profile solution to complex-valued field control, and allows the overall depth of the metaoptic to be on the order of a wavelength.

The compound metaoptic requires reflectionless phase-shifting metasurfaces. Huygens' metasurfaces are excellent candidates since they control the transmission phase and eliminate reflections by maintaining a wave impedance matched to the surrounding medium [8]. However, wide angles of refraction may be required at the two phase planes, resulting in different wave impedances on either side of each metasurface. Reflections from this impedance mismatch can be mitigated using bianisotropic surface parameters: electric, magnetic, and magneto-electric responses. Bianisotropic Huygens' metasurfaces implement a phase shift and serve as impedance matching layers. This allows a reflectionless transition between a wave incident at one angle and refracted to another [9]. It should be noted that where wide-angle refraction is not required (e.g. when wave propagation is predominately paraxial), simple Huygens metasurfaces suffice.

The design of the compound metaoptic involves three general steps. First, the field solution in region II (see Fig. 1) is determined. This solution links the incident local power flux profile S_{inc} to the desired local power flux profile S_{des}. The second step is to compute the electromagnetic parameters of each metasurface. Finally, the metasurfaces can be implemented as asymmetric cascades of electric impedance sheets [6, 9].

A transverse electric (TE) polarization with respect to the metasurface is assumed in this discussion ($\mathbf{E} = E_z\hat{z}$, $\mathbf{H} = H_x\hat{x} + H_y\hat{y}$), but the method equally applies to the transverse magnetic polarization. To simplify the discussion, it is assumed the fields are invariant with respect to z and each metasurface is inhomogeneous along the y-direction. Additionally, field interactions with the phase-discontinuous boundaries are assumed to be reflectionless. A time harmonic progression of of $e^{i\omega t}$ is assumed.

The first step in forming the desired complex-valued field is to determine the phase-shift profiles of each metasurface. Phase-retrieval algorithms are commonly used to determine the phase profile of a wave forming two field amplitude patterns separated by a propagation distance. One such method is the Gerchberg-Saxton algorithm [33, 34], which obtains the phase profiles by forward- and reverse-propagating complex-valued field distributions between the two planes. After each propagation step, the field amplitude is replaced with the correct amplitude profile, while the phase is retained. This action imposes the amplitude profiles as partial constraints for iteratively determining the complex-valued field at each plane. The algorithm iterates until converging to a wavefront phase which creates the two amplitude patterns.

However, directly applying a phase profile to a field amplitude will generally alter the local power flux of the complex-valued field. To ensure the conservation of local power flux, the field amplitude profiles used in the Gerchberg-Saxton algorithm must be modified to exhibit the incident and desired local power flux distributions with each iteration. As a result, the partial constraint conditions of the modified Gerchberg-Saxton algorithm enforce the stipulated local power flux, instead of the electric field amplitude. This substitution of constraint conditions is straightforward since the local power flux and field amplitude are related quantities when the phase is stipulated.

The stipulated local power flux profile at each plane is calculated from the known complex-valued electric fields exterior to the metaoptic, either E_{inc} for the first plane or E_{des} for the second. The electric field plane wave spectrum is calculated and divided by the plane wave TE impedance for each component to determine the plane wave spectrum of the tangential magnetic field H_y. The spatial H_y field is then calculated and used to determine the stipulated local power flux at each boundary.

The original Gerchberg-Saxton algorithm is modified with an additional step to scale the electric field amplitude such that the stipulated local power flux profile

is maintained. Before each propagation step, the phase profile estimate is applied to an assumed electric field amplitude ($|E_{inc}|$ at plane 1, or $|E_{des}|$ at plane 2). The tangential magnetic field is determined from the electric field using the previously described method, allowing the local TE wave impedance (η) for the wave to be calculated. If the local TE wave impedance is assumed to be unchanged after revising the electric field, the complex-valued electric field profile with the stipulated normal power density S and current iteration phase estimate ϕ can be calculated as

$$E = \frac{|\eta|\sqrt{2S}}{\sqrt{\mathrm{Re}\{\eta\}}} e^{j\phi}. \tag{1}$$

This electric field is propagated to the other plane, where the phase is retained and used to calculate another electric field estimate with the stipulated local power flux.

The algorithm is iterated until the propagated fields at each plane exhibit the stipulated normal power density flux profiles (S_{inc} at plane 1 and S_{des} at plane 2), signifying the algorithm has converged. The resulting phase profiles of the field transmitted by metasurface 1 (ϕ_{t1}) and incident on metasurface 2 (ϕ_{i2}) are used to calculate the metasurface phase discontinuities as

$$\phi_{MS1} = \phi_{t1} - \phi_{inc} \tag{2}$$

$$\phi_{MS2} = \phi_{des} - \phi_{i2}. \tag{3}$$

Overall, the modified Gerchberg-Saxton algorithm takes two complex-valued field profiles as inputs (E_{inc} and E_{des}) and produces the phase discontinuity profiles of the two metasurfaces as outputs. Additional details of the modified phase retrieval algorithm are provided in the Supplemental Material [35].

Since this phase retrieval algorithm neglects the evanescent spectrum, complex field transformations are possible that require only propagating spectral content in region II. However, if a solution cannot be obtained at one separation distance L, increasing L often reduces the evanescent content required, and improves the likelihood of a solution. Taking advantage of the evanescent content to form desired complex-valued fields over subwavelength separations would require the excitation of surface waves in addition to propagating waves in region II, and is a direction of future study.

With the tangential field profiles fully determined on both sides of each metasurface, the bianisotropic surface parameters can be calculated. These parameters describe the surface properties needed to convert the wave impedance and phase of the field [6]. Since the field solutions conserve local power flux through the boundaries, these bianisotropic parameters model passive and lossless Huygens' surfaces. The surface parameters can be solved for explicitly in terms of the tangential fields. A derivation is described in the Supplemental Material [35], and is similar to the approach in [36].

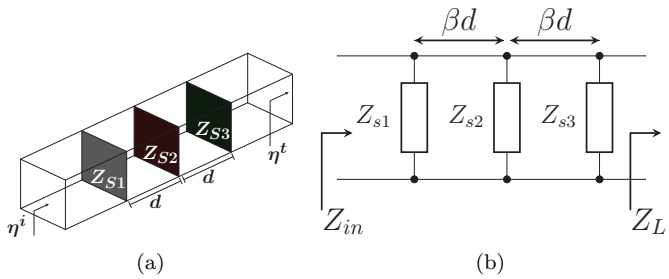

FIG. 2. The unit cell of a bianisotropic Huygens' metasurface is shown in (a), where three sheet impedances (Z_s) are separated by a distance d. The TE wave impedance on either side of the metasurface is denoted as η^i for the incident field and η^t for the transmitted field. The unit cell is modeled by the transmission line circuit shown in (b), where transmission lines separate three shunt impedances.

The field solution of the idealized metaoptic can be observed by explicitly defining the desired electric and magnetic surface current densities in place of the metasurfaces. Figure 1 displays such a *COMSOL Multiphysics* simulation for a metaoptic that expands a normally incident Gaussian beam and imposes a sinusoidal phase profile onto the desired field.

The bianisotropic Huygens' metasurfaces comprising the metaoptic can be implemented by a cascade of electric impedance sheets [6, 7, 9, 37]. Figure 2a shows a Huygens' metasurface unit cell, where three electric impedance sheets are separated by a sub-wavelength distance d. If $Z_{s1} \neq Z_{s3}$, the unit cell exhibits bianisotropic properties. Unit cells of this structure can support equivalent electric and magnetic current densities and be tiled to produce a gradient metasurface.

The metasurface unit cell of Fig. 2a is modeled as the transmission-line circuit in Fig. 2b, which contains three shunt impedances (representing the impedance sheets) separated by electrical lengths of βd. The three variable parameters (shunt impedances) of the circuit model allow control over three desired characteristics. We chose these to be: (1) an input impedance matched to the local incident TE wave impedance ($Z_{in} = \eta_i$), (2) a load impedance matched to the local transmitted TE wave impedance ($Z_L = \eta_t$), and (3) a desired phase delay through the surface. Matching the impedances eliminates reflections, while the desired phase delay implements the phase discontinuity. Since the tangential fields are known adjacent to both metasurfaces, unit cell parameters can be defined to locally satisfy these distributions. The derivation for determining the impedance sheet values as a function of the tangential field characteristics is provided in the Supplemental Material [35].

Using this procedure, the compound metaoptic is designed to transform an incident wave to a desired complex-valued field distribution. We provide two simulation examples where an incident Gaussian beam (beam

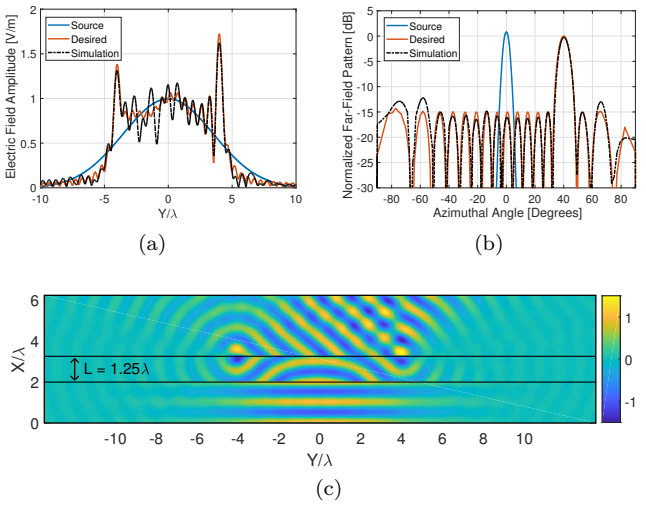

FIG. 3. A compound metaoptic re-shapes an incident Gaussian beam to produce a Dolph-Tchebyscheff far-field pattern pointed towards 40 degrees. The metaoptic performance is shown in (a) as the transmitted electric field amplitude $\lambda/3$ from the metaoptic, (b) as the far-field radiation pattern, and (c) as the real part of the simulated electric field.

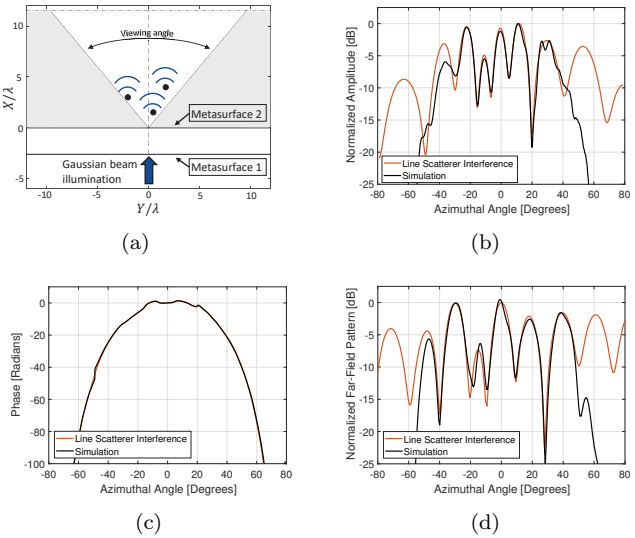

FIG. 4. A compound metaoptic produces the field scattered by three line scatterers arranged as shown in (a). The simulated electric field is compared to the line scatterer interference pattern at a distance of 11.5λ from the metaoptic in (b) as the field amplitude and (c) as the phase. The far-field radiation pattern is shown in (d) for the simulated field distribution and the scatterer interference pattern.

radius of 5λ) is manipulated using a compound metaoptic. Detailed descriptions of the design procedure for each example are provided in the Supplemental Material [35].

In the first example, the incident Gaussian beam is re-shaped to produce a Dolph-Tchebyscheff far-field pattern pointing toward 40 degrees. This far-field pattern exhibits the narrowest main beam since all sidelobes are at the same level [38]. Figure 3a shows the amplitude distribution $\lambda/3$ from the aperture to produce a far-field pattern having sidelobes of -15 dB.

The sheet impedance values of the metasurfaces were calculated for a separation distance of $L = 1.25\lambda$, a unit cell width of $\lambda/16$, and an impedance sheet separation of $d = \lambda/80$. The sheet impedances were modeled as ideal impedance boundaries in the commercial full-wave electromagnetics solver *COMSOL Multiphysics*. Figure 3a shows that the simulated field amplitude just beyond the metaoptic matches the desired field amplitude. Figure 3b shows the far-field pattern closely matches the desired Dolph-Tchebyscheff pattern. Each of the sidelobes are nearly -15 dB relative to the main lobe, and all pattern nulls are located at the correct angles. Figure 3c shows the simulated electric field, within and surrounding the metaoptic. The first metasurface transforms the local power flux profile across the separation distance L, and the second metasurface points the main beam toward 40 degrees. Figure 3c confirms that there are nearly no reflections from the compound metaoptic.

In the second example, a compound metaoptic is designed to radiate a field identical to the first-order scattered field from three line scatterers. Essentially, the compound metaoptic realizes a simple complex-valued hologram of the scatterers. The virtual line scatterers are in the region beyond the metaoptic, (see Fig. 4a) and excited by a plane wave traveling in the $-x$ direction. The plane wave spectrum of the field generated by each scatterer is summed to obtain the total scattered plane wave spectrum along the $x = 0$ plane. A windowing function was applied to this spectrum such that the scattered field is visible over a viewing angle between ± 40 degrees. The desired spatial electric field distribution is obtained from the windowed plane wave spectrum, and used to design the compound metaoptic.

The metaoptic was designed with a separation distance of $L = 2.25\lambda$, a unit cell dimension of $\lambda/16$, and an impedance sheet spacing of $d = \lambda/60$. Figure 4b and Fig. 4c compare the simulated electric field amplitude and phase, respectively, at a distance of 11.5λ from the metaoptic with the interference pattern of the three line scatterers. We see that the electric field produced by the metaoptic closely matches, in amplitude and phase, the ideal interference pattern of the three line scatterers over a field of view of ± 40 degrees. This is achieved even at short distances from the metaoptic. Fig. 4d shows that the far-field pattern also closely matches the true interference pattern over the desired azimuthal range. This demonstrates that the compound metaoptic is capable of reconstructing the field scattered from known objects in amplitude and phase.

The proposed compound metaoptic uses two local power flux conserving, phase-discontinuous metasurfaces

to mold the available power from a source into a desired complex-valued field profile. The bianisotropic properties of these constitutive Huygens' metasurfaces also allow the metaoptic to have a wavelength-scale thickness.

Compound metaoptics may find applications in 3D holographic display technology. This approach also presents a new design paradigm for electronically scanned antennas. Conventional approaches at microwave/millimeter-wave frequencies utilize phased arrays, where phase shifters provide beam steering and amplifiers/attenuators provide beam shaping. Such a method becomes increasingly difficult to implement at shorter wavelengths due to transistor cutoff frequencies and array feeding network losses. The proposed approach is especially attractive at millimeter-wave frequencies and beyond, given that it allows beam shaping (amplitude control) and beam steering (phase control) simply by using two phase planes.

This work was supported by the National Science Foundation Graduate Research Fellowship Program under Grant No. DGE 1256260 and the Office of Naval Research under Grant No. N00014-15-1-2390.

[1] C. L. Holloway, E. F. Kuester, J. A. Gordon, J. O'Hara, J. Booth, and D. R. Smith, IEEE Antennas and Propagation Magazine **54**, 10 (2012).
[2] H.-T. Chen, A. J. Taylor, and N. Yu, Reports on Progress in Physics **79**, 076401 (2016).
[3] H. Hsiao, C. H. Chu, and D. P. Tsai, Small Methods **1**, 1600064.
[4] N. Yu and F. Capasso, Nature Materials **13**, 139 (2014).
[5] A. V. Kildishev, A. Boltasseva, and V. M. Shalaev, Science **339** (2013).
[6] C. Pfeiffer and A. Grbic, Phys. Rev. Applied **2**, 044011 (2014).
[7] F. Monticone, N. M. Estakhri, and A. Alù, Phys. Rev. Lett. **110**, 203903 (2013).
[8] C. Pfeiffer and A. Grbic, Phys. Rev. Lett. **110**, 197401 (2013).
[9] J. P. S. Wong, A. Epstein, and G. V. Eleftheriades, IEEE Antennas and Wireless Propagation Letters **15**, 1293 (2016).
[10] K. E. Chong, L. Wang, I. Staude, A. R. James, J. Dominguez, S. Liu, G. S. Subramania, M. Decker, D. N. Neshev, I. Brener, and Y. S. Kivshar, ACS Photonics **3**, 514 (2016).
[11] L. Huang, X. Chen, H. Mhlenbernd, H. Zhang, S. Chen, B. Bai, Q. Tan, G. Jin, K.-W. Cheah, C.-W. Qiu, J. Li, T. Zentgraf, and S. Zhang, Nature Communications **4** (2013).
[12] Q. Wang, X. Zhang, Y. Xu, J. Gu, Y. Li, Z. Tian, R. Singh, S. Zhang, J. Han, and W. Zhang, Scientific Reports **6** (2016).
[13] X. Ni, A. V. Kildishev, and V. M. Shalaev, Nature Communications **4** (2013).
[14] C. Chang, J. Xia, L. Yang, W. Lei, Z. Yang, and J. Chen, Appl. Opt. **54**, 6994 (2015).
[15] C. Chang, Y. Qi, J. Wu, J. Xia, and S. Nie, Opt. Express **25**, 6568 (2017).
[16] S. Yu, X. Piao, and N. Park, Phys. Rev. Lett. **120**, 193902 (2018).
[17] G. Gok and A. Grbic, Phys. Rev. Lett. **111**, 233904 (2013).
[18] B. B. Tierney and A. Grbic, IEEE Transactions on Antennas and Propagation **63**, 2439 (2015).
[19] G. Minatti, M. Faenzi, E. Martini, F. Caminita, P. D. Vita, D. Gonzlez-Ovejero, M. Sabbadini, and S. Maci, IEEE Transactions on Antennas and Propagation **63**, 1288 (2015).
[20] G. Minatti, F. Caminita, E. Martini, M. Sabbadini, and S. Maci, IEEE Transactions on Antennas and Propagation **64**, 3907 (2016).
[21] A. Epstein and G. V. Eleftheriades, IEEE Transactions on Antennas and Propagation **62**, 5680 (2014).
[22] B. O. Raeker and S. M. Rudolph, IEEE Antennas and Wireless Propagation Letters **15**, 1101 (2016).
[23] B. O. Raeker and S. M. Rudolph, IEEE Transactions on Antennas and Propagation **64**, 5243 (2016).
[24] N. Yu, P. Genevet, M. A. Kats, F. Aieta, J.-P. Tetienne, F. Capasso, and Z. Gaburro, Science **334**, 333 (2011).
[25] L. Liu, X. Zhang, K. Mitchell, X. Su, N. Xu, C. Ouyang, Y. Shi, J. Han, W. Zhang, and S. Zhang, Advanced Materials **26**, 5031 (2014).
[26] Z. Li, H. Cheng, Z. Liu, S. Chen, and J. Tian, Advanced Optical Materials **4**, 1230 (2016).
[27] G.-Y. Lee, G. Yoon, S.-Y. Lee, H. Yun, J. Cho, K. Lee, H. Kim, J. Rho, and B. Lee, Nanoscale **10**, 4237 (2018).
[28] D.-H. Kwon, G. Ptitcyn, A. Díaz-Rubio, and S. A. Tretyakov, Phys. Rev. Applied **9**, 034005 (2018).
[29] B. O. Zhu and Y. Feng, IEEE Transactions on Antennas and Propagation **63**, 5500 (2015).
[30] A. Jesacher, C. Maurer, A. Schwaighofer, S. Bernet, and M. Ritsch-Marte, Opt. Express **16**, 2597 (2008).
[31] C. Wu, J. Ko, J. R. Rzasa, D. A. Paulson, and C. C. Davis, Appl. Opt. **57**, 2337 (2018).
[32] A. Siemion, M. Sypek, J. Suszek, M. Makowski, A. Siemion, A. Kolodziejczyk, and Z. Jaroszewicz, Opt. Lett. **37**, 5064 (2012).
[33] R. Gerchberg and W. Saxton, Optik **35**, 237 (1972).
[34] J. R. Fienup, Optical Engineering **19**, 19 (1980).
[35] See Supplemental Material at [URL will be inserted by publisher], .
[36] A. Epstein and G. V. Eleftheriades, IEEE Transactions on Antennas and Propagation **64**, 3880 (2016).
[37] C. Pfeiffer, N. K. Emani, A. M. Shaltout, A. Boltasseva, V. M. Shalaev, and A. Grbic, Nano Letters **14**, 2491 (2014).
[38] E. C. Jordan and K. G. Balmain, *Electromagnetic Waves and Radiating Systems* (Prentice-Hall, Inc.; Englewood Cliffs, New Jersey, 1968).